

Characteristics of the RAW-Filtered Leapfrog Time-Stepping Scheme in the Ocean General Circulation Model

CHIH-CHIEH YOUNG

Department of Atmospheric Sciences, National Taiwan University, and Research Center for Environmental Changes, Academia Sinica, Taipei, Taiwan

YU-CHIAO LIANG AND YU-HENG TSENG*

Department of Atmospheric Sciences, National Taiwan University, Taipei, Taiwan

CHUN-HOE CHOW

Research Center for Environmental Changes, Academia Sinica, Taipei, Taiwan

(Manuscript received 13 November 2012, in final form 13 June 2013)

ABSTRACT

The Robert–Asselin–Williams (RAW) filtered leapfrog scheme is implemented and tested in the Taiwan multiscale community ocean model (TIMCOM). The characteristics of the RAW filter are carefully examined through two benchmark tests (the classical model problem-oscillation equation with further consideration of the dissipation effect, and the 1D linearized shallow-water equations). Particularly, the effect of the RAW filter upon the $2\Delta x$ wave instability due to spatial truncation errors is addressed. TIMCOM is then applied to simulate the coastally trapped internal Kelvin waves and global ocean circulations, showing the practical improvement over the Robert–Asselin (RA) filter in the short- and long-term model integrations. The large mean differences in some major current systems suggest the potential impacts on the oceanic instability where the numerical dissipation may interfere with the physical one. The characteristic analysis and model results here indicate the significant advantage of the RAW-filtered leapfrog time-stepping scheme for accurate ocean modeling.

1. Introduction

Accurate and efficient global ocean modeling plays an important role in the understanding of climate dynamics and future projections of climate change. Oceanic circulation driven by wind forcing and density gradients (attributed by thermohaline differences) can redistribute solar energy and affect the global climate system (Gill 1982). Particularly, the thermohaline circulation, which consists of surface and deep-water currents, may possibly trigger severe climate change events (Wood

et al. 1999; Solomon et al. 2007). To complete more realistic climate modeling, accurate simulation of global ocean circulation is essential, in addition to the satellite remotely sensed data and in situ measurements.

The time-stepping schemes used in general circulation models are very critical to resolve transient phenomenon. During the past few decades, continuous efforts have been devoted to developing various explicit/implicit/iterative time-stepping methods from a low to a higher order of accuracy for the compromise between realistic simulation and computational cost (e.g., Mesinger and Arakawa 1976; Pfeffer et al. 1992; Teixeira et al. 2007). The readers can further refer to Durran (1991) for a thorough review of common approaches such as the Matsuno scheme (Euler-backward iteration), the leapfrog scheme, the Adams–Bashforth family of schemes, and the Runge–Kutta types. Compared to more accurate alternatives (Durran 1991; Kar 2006), the (filtered) leapfrog time-stepping scheme (Asselin 1972) has the

* Current affiliation: Climate and Global Dynamics Division, National Center for Atmospheric Research, Boulder, Colorado.

Corresponding author address: Yu-Heng Tseng, Climate and Global Dynamics Division, National Center for Atmospheric Research, 1850 Table Mesa Dr., Boulder, CO 80305.
E-mail: ytseng@ucar.edu

advantages of low computational cost, low run-time storage, and ease of implementation. As a consequence, it has prevailed over the years in the communities of oceanic and atmospheric sciences [e.g., the Modular Ocean Model (MOM) of the Geophysical Fluid Dynamics Laboratory (GFDL), the Parallel Ocean Program of Los Alamos Climate Ocean model, the Nucleus for European Modeling of the Ocean (NEMO), the Community Atmosphere Model (CAM) of the National Center for Atmosphere Research (NCAR), and many others].

The unfiltered leapfrog scheme is commonly not used in practice because of its severe time-splitting instability in many nonlinear cases (i.e., a spurious oscillation associated with the undamped computational mode; Asselin 1972). Generally, three types of methods have been proposed to control these effects. The first approach is to periodically reinitialize the leapfrog solution using a two-time-level method in one single step (e.g., applying a single Matsuno step after every 11 leapfrog steps; Pfeffer et al. 1992). However, the computational mode is not fully eliminated and may become unstable for longer integrations. Second, coupling with other second-order approaches per time step [e.g., the leapfrog-trapezoidal (Kurihara 1965) or the leapfrog–Adams–Bashforth (Magazenkov 1980) scheme] yields effective suppression of the computational mode, but leads to a costly iterative process. Also, major problems for fast modes remain, such as the inertia–gravity waves that are involved in geostrophic adjustment dynamics. The last strategy at almost no additional computational cost is to utilize a time filter in the time-advancing procedure [e.g., the Robert–Asselin (RA) filtered leapfrog scheme (Asselin 1972) or its special case, the weighted filtered leapfrog-trapezoidal scheme (Dietrich and Wormeck 1985; Roache and Dietrich 1988)]. Such an effective RA filtering approach is commonly used nowadays. However, two major problems remain: (i) the damping of the physical mode in the solutions, and (ii) the degradation of the formal accuracy to first order.

Williams (2009) recently proposed a simple but useful modification of the RA filter, referred to as the Robert–Asselin–Williams (RAW) filter. Using the RAW filter, we can effectively suppress the spurious computational mode in the original leapfrog scheme with a (nearly) conserved mean state, achieving (almost) third-order accuracy for wave amplitude errors while maintaining second-order phase accuracy. In Williams (2009), the basic behavior of the RAW filter was analyzed and demonstrated using the oscillation equation (Durran 1991). It was further implemented and tested in the Simplified Parameterizations, Primitive Equation Dynamics (SPEEDY) atmospheric general circulation model (Molteni 2003) recently, revealing almost identical

monthly climatology and significant improvement in the 5-day weather forecasts without the need of reparameterization (Amezcuca et al. 2011).

In this paper, the RAW-filtered leapfrog time-stepping scheme is evaluated from several aspects and applied to a recently developed oceanic general circulation model, the Taiwan multiscale community ocean model (TIMCOM; Young et al. 2012), which will further serve as a key component in an earth system modeling framework. We first examine the characteristics of the RAW filter using the classical model problem (i.e., oscillation equation with further consideration of the dissipation effect) and the 1D linearized shallow-water equations. The impacts of RAW filter on computational $2\Delta x$ wave instability due to spatial truncation errors are further studied. The analysis also suggests appropriate filtering parameters and time step (determined by Courant number) for accurate ocean general circulation modeling. We then apply TIMCOM to simulate internal Kelvin waves (Beletsky et al. 1997) and global oceanic circulations (Tseng and Chien 2011), showing the practical improvement over the RA filter in the short- and long-term model integrations. Section 2 analyzes the key characteristics of the RAW filter. Section 3 contains a brief description of TIMCOM. Section 4 presents the model results and discussion. A short summary is given in section 5.

2. Characteristics of the third-order RAW-filtered leapfrog scheme

The RAW-filtered leapfrog scheme was proposed to resolve the time-splitting issue and provide some features of third-order accuracy in amplitude (Williams 2009). Compared with the original RA filter, the key idea is to conserve the mean state of variables averaged over three successive time levels in order to minimize the numerical damping of the physical mode while reducing the curvature to remove spurious oscillation (i.e., computational mode). The RAW-filtered leapfrog scheme implements the simple leapfrog method for $du/dt = f(u)$ using filtered values in both backward/centered time levels that are updated with the smoothing displacements αd and $(1 - \alpha)d$ when marching time from $t = t$ to $t = t + \Delta t$. It can be written as follows:

$$u^{n+1} = \overline{\overline{u^{n-1}}} + 2\Delta t \times f(\overline{u^n}), \tag{1}$$

$$\overline{u^n} = \overline{u^n} + \alpha d = \left[\overline{u^n} + \alpha \frac{v}{2} (\overline{u^{t-1}} - 2\overline{u^n} + u^{n+1}) \right], \tag{2}$$

$$\begin{aligned} \overline{u^{n+1}} &= u^{n+1} - (1 - \alpha)d \\ &= \left[u^{n+1} - (1 - \alpha) \frac{v}{2} (\overline{\overline{u^{n-1}}} - 2\overline{u^n} + u^{n+1}) \right], \quad (3) \end{aligned}$$

where the superscripts $n - 1$, n , and $n + 1$ represent the backward/centered/forward time levels used in the leapfrog scheme and Δt is the time step; the parameter v determines the smoothing displacement and is usually chosen to be $O(0.01\text{--}0.3)$ to eliminate the time splitting error without losing accuracy (Asselin 1972; Durran 1991; Kantha and Clayson 2000); the other parameter α , bounded between 0 and 1, controls the relative contributions between the two time levels. It is clear that the three stages, Eqs. (1)–(3), in the scheme yield a recursive procedure (see Williams 2009 for details). The variable u is a provisional value obtained by Eq. (1) during the current time step. The single overbar denotes another singly filtered provisional value updated by Eq. (3) during the current time. The double overbar denotes the doubly filtered definitive value updated by Eq. (2) during the next time step. In the family of the RAW filters, the case $v = 0$ turns to the pure leapfrog scheme so that the variables in Eqs. (2)–(3) are directly updated without additional correction. The case $\alpha = 1$ yields the traditional RA filter. The special case of $\alpha = 0.5$ maintaining the three-time-level mean state can greatly improve the amplitude error, but suffers from the issue of unconditional instability (see the detailed analysis below). Here, we examine the numerical characteristics of the RAW filter and its spatial dependency, which is essential before further implementation into any oceanic (or atmospheric) general circulation models.

a. Classical model problem-oscillation equation

Consider the classical benchmark test in numerical analysis: $du/dt = \lambda u$, where the complex constant $\lambda = \lambda_R + i\lambda_I$ determines the amplification ($\lambda_R > 0$)/damping ($\lambda_R < 0$) and frequency (arbitrary λ_I) of the oscillation (Durran 1991). Discretizing the above equation by the RAW-filtered leapfrog scheme in Eqs. (1)–(3) gives the amplification factors for physical (A_+) and computational (A_-) modes:

$$\begin{aligned} A_{\pm} &= \frac{u^{n+1}}{u^n} = c_1 + c_2(\lambda\Delta t) \\ &\pm \sqrt{(1 - c_1)^2 + 2(1 - c_1)(1 - c_2)(\lambda\Delta t) + (c_2\lambda\Delta t)^2}, \quad (4) \end{aligned}$$

where $c_1 = v/2$ and $c_2 = 1 - (1 - \alpha)(v/2)$.

Figure 1 shows the stability analysis in a complex plane for the cases of $v = 0.1, 0.2, \text{ and } 0.5$, and $\alpha = 0, 0.5$,

and 1. The stable region (i.e., bounded by $|A_{\pm}| \leq 1$) expands/shifts with increasing v and reducing α , similar to the left column in Fig. 3 of Durran and Blossey (2012). We also compare the numerical amplification factors (ranging from 0.9 to 1). For the physical mode A_+ , the amplification factors decrease along the negative real axis (i.e., reducing the real part of $\lambda\Delta t$). The concave ($\alpha > 0.5$) and convex ($\alpha \leq 0.5$) curved contours indicate numerical damping and amplification, respectively, in comparison with the exact solution $A_{\text{exact}} = \exp(\lambda\Delta t)$ that is straight and parallel to the imaginary axis. The computational mode A_- presents an opposite behavior. In contrast to case $\alpha = 1$, $\alpha \leq 0.5$ yields a smaller amplification factor at a given $\lambda\Delta t$, providing more effective suppression for the spurious oscillation.

The accuracy of the RAW filter is further analyzed using a pure oscillation solution with period T (or frequency $\omega = 2\pi/T$). We test a range of time steps Δt from $T/20$ to $T/2560$ (or dimensionless time step $\omega\Delta t$ from 0.314 to 0.002). Figure 2 compares the amplification factor A_+ and relative amplitude error (i.e., $\varepsilon_a = |a_{\text{model}} - a_{\text{exact}}|/a_{\text{exact}}$ vs $\omega\Delta t$). Amplification factors asymptotically approach to the exact solution from both sides as the time step decreases (see Fig. 2a), indicating the unconditionally stable (unstable) property for the case $\alpha = 1$ ($\alpha \leq 0.5$). Note that the case of $\alpha = 0.5$ converges rapidly to the unity. The relative amplitude errors in Figs. 2b–d further reveal the third-order accuracy of $\alpha = 0.5$, unlike the rest first-order cases. The relative amplitude error is also sensitive to the smoothing parameter v , which should be small for better accuracy, consistent with the earlier studies (e.g., Durran 1991). The other parameter α has been suggested to be 0.53 (i.e., a weighted blend of the third-order and first-order filters) to provide the conditional stability across $0 \leq \omega\Delta t \leq \sqrt{8(\alpha - 0.5)(1 - 0.5v)} = 0.47$ (see Fig. 2a) and almost third-order (strictly first order) amplitude accuracy for the practical applications (Williams 2009). Note that a smaller α (e.g., 0.51) constrains the applicable range of $\omega\Delta t$ (e.g., only up to 0.27) and a larger one (e.g., 0.55) increases the computation error (e.g., $\varepsilon_{\alpha=0.55} = 3.9\varepsilon_{\alpha=0.53}$ at $\omega\Delta t = 0.4$). Here, the phase errors are not discussed because the accuracy remains second order.

In addition, we further analyze the impacts of physical dissipation, which make the initial amplitude reduce to a certain degree (e.g., 80%) over several wave periods (e.g., 10T). Given the wave period with a damping condition, the complex constant of model problem can be determined [i.e., $\lambda = \lambda_R + i\lambda_I = \ln(0.8)/10T + i(2\pi/T)$]. Figure 3 presents the amplification factor A_+ , relative amplitude error, and time series of the simulations with $\alpha = 0, 0.5, \text{ and } 0.53$, and 1 based on a fixed $v = 0.1$ and a range of Δt . Overall, the behavior of amplification

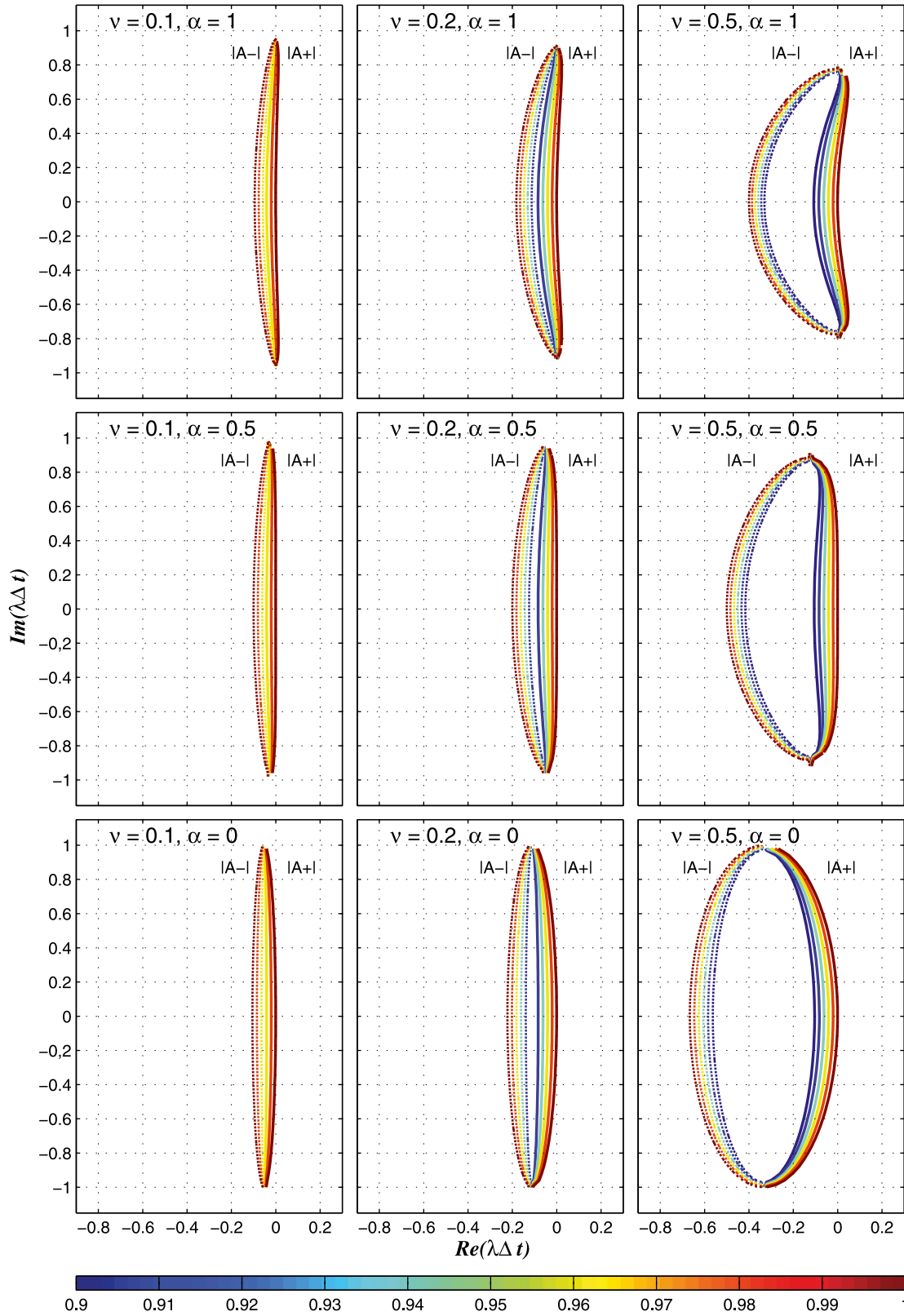


FIG. 1. Stability analysis including numerical amplification factors of physical (A_+) and computational modes (A_-) for the family of RAW filter.

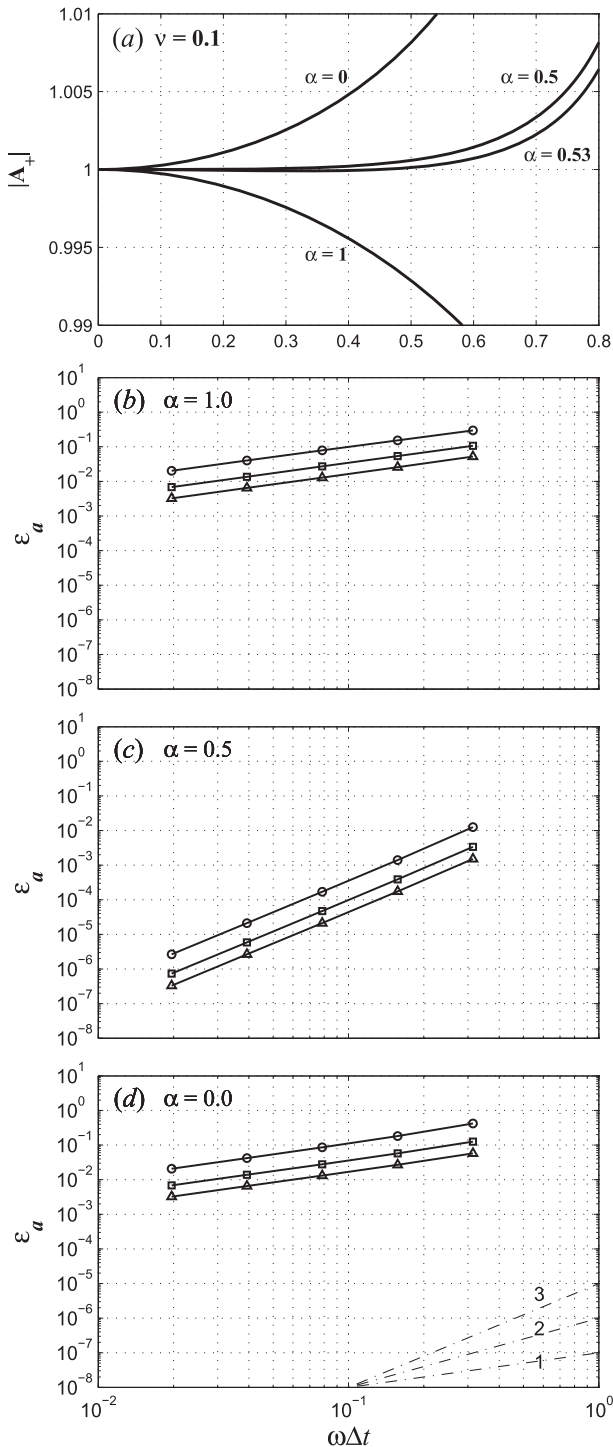


FIG. 2. Accuracy analysis including (a) the numerical amplification factor of physical mode A_+ and (b)–(d) relative amplitude errors ϵ_u for the family of RAW filter (triangles: $v = 0.1$, squares: $v = 0.2$, and circles: $v = 0.5$).

factors (Fig. 3a) is similar to that in Fig. 2a except for a downward shift due to the dissipation effect (amplitude damping). As a result, the case of $\alpha = 0.5$ becomes conditionally stable ($\omega\Delta t < 0.7$) with an underestimated damping and the rest cases have the same stability characteristics. The relative amplitude errors clearly show the convergent order for each case. For the cases of first-order accuracy, $\alpha = 0$ and $\alpha = 1$ are overlapped but the suggested $\alpha = 0.53$ has an order of magnitude smaller error. The special case $\alpha = 0.5$ results in the second-order overall accuracy due to the combination of the third-order accuracy in oscillation and the second-order accuracy in dissipation that can be shown by the Taylor expansion of Eq. (4): $A_+(\alpha = 0.5, v, \lambda\Delta t) = 1 + \lambda\Delta t + 1/2(\lambda\Delta t)^2 - [v/8(1 - v/2)](\lambda\Delta t)^3 + O[(\lambda\Delta t)^4]$. Using the time step $\Delta t = T/40$ ($\omega\Delta t = 0.16$), the result simulated by $\alpha = 0.53$ or 0.5 agrees well with the exact solution. The case of $\alpha = 1$ (i.e., the RA filter) overestimates the dissipation (i.e., 60% of the initial amplitude u_0 over 10T) while the case $\alpha = 0$ results in totally unrealistic amplification (Fig. 3c).

b. One-dimensional linearized shallow-water equations

The one-dimensional linearized shallow-water equations are then used to diagnose the performance of RAW filter. Viscosity is excluded to identify numerical damping (amplification). In the staggered C grids, the leapfrog finite-difference equations for surface elevation η and velocity u are

$$\frac{\eta_m^{n+1} - \eta_m^{n-1}}{2\Delta t} = -h_i \frac{u_{m+1/2}^n - u_{m-1/2}^n}{\Delta x}, \tag{5}$$

$$\frac{u_{m+1/2}^{n+1} - u_{m+1/2}^{n-1}}{2\Delta t} = -g \frac{\eta_{m+1}^n - \eta_m^n}{\Delta x}, \tag{6}$$

where h is the mean water depth and g is gravity. Substituting the wave-type solutions $\eta_m^{n+1} = \eta_0^{n+1} \exp(ikm\Delta x)$ and $u_{m+1/2}^{n+1} = u_0^{n+1} \exp[ik(m + 1/2)\Delta x]$, Eqs. (5)–(6) can be rewritten as

$$\begin{aligned} \frac{\eta_0^{n+1} - \eta_0^{n-1}}{2\Delta t} &= -h_i u_0^n \frac{\exp(ik\Delta x/2) - \exp(-ik\Delta x/2)}{\Delta x} \\ &= -ih_i u_0^n X, \end{aligned} \tag{7}$$

$$\begin{aligned} \frac{u_0^{n+1} - u_0^{n-1}}{2\Delta t} &= -g \eta_0^n \frac{\exp(ik\Delta x/2) - \exp(-ik\Delta x/2)}{\Delta x} \\ &= -ig \eta_0^n X, \end{aligned} \tag{8}$$

where the variables with subscript 0 represent their amplitudes; k is the wavenumber; and X is $\sin(k\Delta x/2)/(\Delta x/2)$. Both variables are smoothed using the RAW

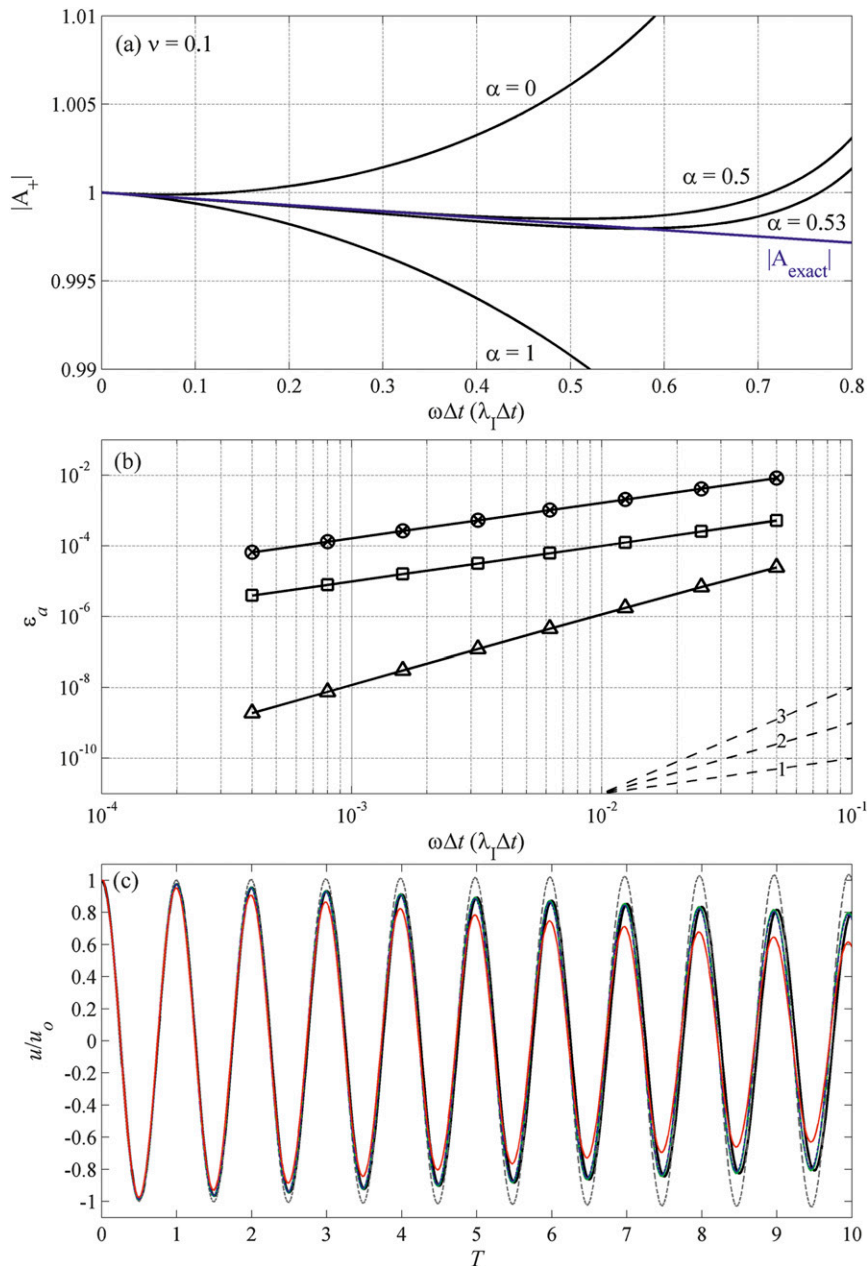


FIG. 3. Accuracy analysis for oscillation with dissipation: (a) the numerical amplification factor of physical mode A_+ , (b) the relative amplitude errors ϵ_a for the family of RAW filter (\times : $\alpha = 0$, triangles: $\alpha = 0.5$, squares: $\alpha = 0.53$, and circles: $\alpha = 1$), and (c) the associated time series (black lines: exact solutions, gray dashed lines: $\alpha = 0$, blue dashed lines: $\alpha = 0.53$, green solid lines: $\alpha = 0.5$, and red lines: $\alpha = 1$).

filter before marching to the next time step. Using the eigenvalue analysis similar to Eqs. (8)–(10) in Sun (2010) and some mathematical manipulations (more details in

Sun 2010), we can derive the repeated amplification factors for the surface elevation and velocity in a similar form:

$$A_{\pm} = c_1 + c_2(\pm C\Delta T) \pm \sqrt{(1 - c_1)^2 + 2(1 - c_1)(1 - c_2)(\pm C\Delta T) + [c_2(\pm C\Delta T)]^2}, \tag{9}$$

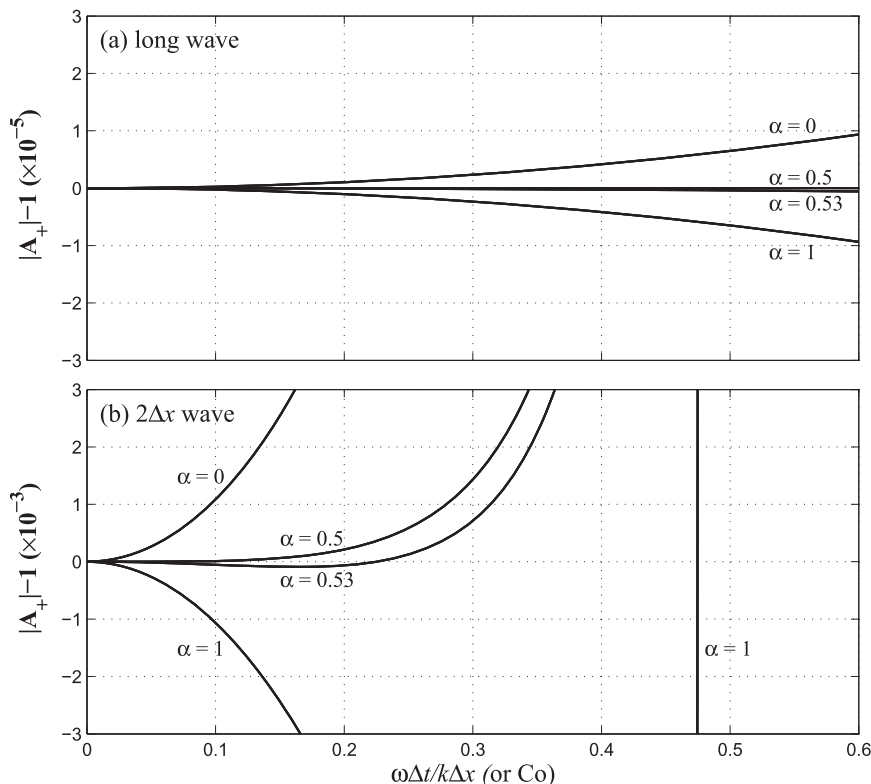


FIG. 4. Accuracy analysis of the numerical amplification factor A_+ with $\nu = 0.1$ for (a) the incident long wave and (b) the computational $2\Delta x$ wave.

where $\pm C = \pm\sqrt{gh}$ represents the downstream (upstream) propagating wave speed, $\Delta T = i\Delta tX$, and $C\Delta T = i(C\Delta t/\Delta x)2\sin(k\Delta x/2) = i(\omega\Delta t/k\Delta x)2\sin(k\Delta x/2)$.

To further examine the capability of RAW-filtered leapfrog scheme, we simulate linear long waves (with wavelength $\lambda = 10\,000$ km and amplitude $a = 0.001$ h) traveling through a flat bottom (water depth $h = 4000$ m) over a geophysical-scale distance (e.g., $L = 3\lambda = 30\,000$ km). The corresponding wave speed C and period T are 198 m s^{-1} and 14 h, respectively. Given a spatial resolution $\Delta x = \lambda/200 = 50$ km (around 0.5°), the time step Δt can be determined by the Courant number $Co = C\Delta t/\Delta x = \omega\Delta t/k\Delta x$. Periodic boundary conditions are applied. Figure 4 shows the relationship between the absolute amplitude error ($|A_+| - 1$) and Courant number Co . If $Co < 0.5$, the magnitude of error is $O(10^{-5})$ for the long waves calculated using $\nu = 0.1$ and any chosen α . With a fixed Co , reducing grid size yields a smaller $C\Delta T = iCo2\sin(k\Delta x/2)$ and becomes more accurate. Notice that the $2\Delta x$ wave instability due to amplification of spatial truncation errors can be significantly enhanced by a factor around $O(1.3)$ at $Co = 0.5$, which is neutral in the pure leapfrog scheme (Durrant 1991; Sun 2010). Figure 4b shows that, for a smaller Co (e.g., $Co < 0.35$), the first-order accurate case of $\alpha = 1$ can effectively damp out the

noise of $2\Delta x$ wave while the rest of the parameters ($\alpha \leq 0.5$) can reduce the numerical instability to the order of 10^{-3} in magnitude. Also, the convergent behaviors in the RA and RAW filters are qualitatively different [i.e., two branches in the case of $\alpha = 1$ with the singularity point (beyond the lower bond of the axis) at $Co = 0.5(1 - \nu/2)$ or a smooth transition for the other cases]. This founding is consistent with Fig. 4 in Williams (2009). Overall, our analysis further suggests $Co \leq 0.2$ should be used for the practical applications, while the optimal filtering parameters $\alpha = 0.53$ and $\nu = 0.1$ remain as a result of the analogy between the Eqs. (9) and (4). Figure 5 shows the spatial profile of surface elevation and its underlying velocity field at $t = 150T$ (about 2.5 months). Using the recommended settings, the simulation (blue dashed lines) almost converges to the analytical solution with excellent agreement, while evident numerical damping (15% decreasing of the initial amplitude) and apparent $2\Delta x$ wave instability can be found in the cases of $\alpha = 1$ (red dashed lines) and $\alpha = 0.5$ (green zigzag lines), respectively.

3. TIMCOM model description

The RAW filter is further implemented in an oceanic general circulation model, TIMCOM (see Young et al.

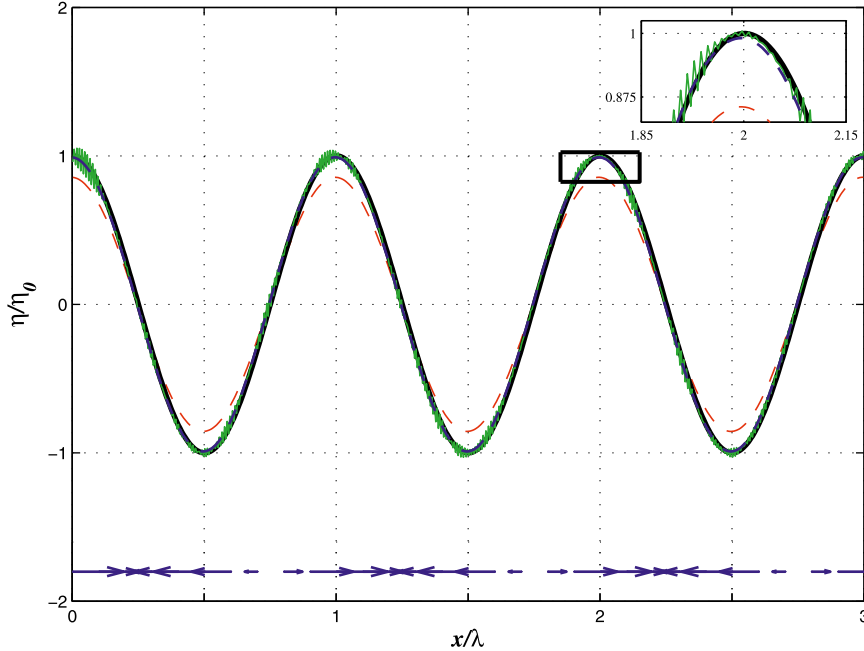


FIG. 5. The modeled spatial profiles (lines) and underlying velocity field (lines with arrows) at $t = 150T$ (black lines: exact solutions, red dashed lines: $\alpha = 1.0$, green solid lines: $\alpha = 0.5$, and blue dashed lines: $\alpha = 0.53$).

2012). To simulate the motions of an incompressible, stratified fluid, TIMCOM solves the 3D primitive equations with the Boussinesq and hydrostatic assumptions in the Cartesian or spherical coordinate (λ, ϕ, z, t) :

$$\nabla_3 \cdot \mathbf{u} = 0, \quad (10)$$

$$u_t + \nabla_3 \cdot (u\mathbf{u}) - (f + u \tan\phi/R)v = -p_\lambda/(\rho_0 R \cos\phi) + \nabla_2 \cdot A_m \nabla_2 u + (K_m u_z)_z, \quad (11)$$

$$v_t + \nabla_3 \cdot (v\mathbf{u}) + (f + u \tan\phi/R)u = -p_\phi/(\rho_0 R) + \nabla_2 \cdot A_m \nabla_2 v + (K_m v_z)_z, \quad (12)$$

$$p_z = -\rho g, \quad (13)$$

$$T_t + \nabla_3 \cdot (T\mathbf{u}) = \nabla_2 \cdot A_h \nabla_2 T + (K_h T_z)_z, \quad (14)$$

$$S_t + \nabla_3 \cdot (S\mathbf{u}) = \nabla_2 \cdot A_h \nabla_2 S + (K_h S_z)_z, \quad (15)$$

where $\mathbf{u} = (u, v, w)$ is the velocity vector; $p = p_s + p_b$ is the total pressure consisting of the surface pressure p_s and baroclinic pressure $p_b = g \int_z^0 \rho dz$; ρ (ρ_0) is the in situ (reference) density; T and S are potential temperature and salinity, respectively; f is the Coriolis parameter; g is the gravitational acceleration; A_m , A_h , K_m , and K_h are the eddy viscosity and diffusivity in the horizontal and vertical planes, respectively; and the divergence operator is $\nabla_3 = \nabla_2 + (\cdot)_z \mathbf{k} = (1/R \cos\phi)(\cdot)_\lambda \mathbf{i} + (1/R)(\cdot)_\phi \mathbf{j} + (\cdot)_z \mathbf{k}$. Either free-surface or rigid-lid approximation can be

used at the ocean surface for a broad range of applications (Young et al. 2012).

The governing equations in TIMCOM are now solved using the third-order RAW-filtered leapfrog scheme (Williams 2009) and the fourth-order spatial approximation (Sanderson and Brassington 1998). The computational domain can be nonuniformly divided into control volumes along i, j , and k directions. Flow variables are arranged on a mixed Arakawa A (collocated) and C (staggered) grid (i.e., the cell-averaged variables $u_{i,j,k}$, $v_{i,j,k}$, $S_{i,j,k}$, $T_{i,j,k}$, $p_{i,j,k}$, $\rho_{i,j,k}$, and the face-averaged velocities $U_{i+1/2,j,k}$, $V_{i,j+1/2,k}$, $W_{i,j,k+1/2}$). The overall predictor-corrector procedure (Young et al. 2012), is briefly presented as follows.

- 1) Predictor step: To obtain the intermediate velocities, momentum equations are discretized at cell centers using centered time-stepping for advection and fourth-order pressure gradient, and forward time stepping for diffusion:

$$\begin{aligned} & \frac{\tilde{u}_{i,j,k}^{n+1} - u_{i,j,k}^{n-1}}{2\Delta t} + \nabla_3 \cdot (u^n \mathbf{u}^n) \\ &= -\frac{(p_s^{n-1} + p_b^n)_\lambda}{\rho_0 R \cos\phi} + \nabla_2 \cdot A_m \nabla_2 u^{n-1} \\ & \quad + [K_m (u^{n-1})_z]_z, \end{aligned} \quad (16)$$

where

$$\nabla_3 \cdot (u^n \mathbf{u}^n) = \frac{U_{i+1/2,j,k}^n u_{i+1/2,j,k}^{n+1} - U_{i-1/2,j,k}^n u_{i-1/2,j,k}^{n+1} + V_{ij+1/2,k}^n u_{ij+1/2,k}^{n+1} - V_{ij-1/2,k}^n u_{ij-1/2,k}^{n+1}}{R \cos \phi \Delta \lambda_i} + \frac{W_{ij,k+1/2}^n u_{ij,k+1/2}^{n+1} - W_{ij,k-1/2}^n u_{ij,k-1/2}^{n+1}}{\Delta z_k},$$

$$[p_{s(b)}^{n-1(n)}]_\lambda = \frac{[p_{s(b)}]_{i-2,j,k}^{n-1(n)} - 8[p_{s(b)}]_{i-1,j,k}^{n-1(n)} + 8[p_{s(b)}]_{i+1,j,k}^{n-1(n)} - [p_{s(b)}]_{i+2,j,k}^{n-1(n)}}{12\Delta \lambda_i},$$

$$\nabla_2 \cdot A_m \nabla_2 u^{n-1} = \frac{A_m}{R^2} \left(\frac{u_{i+1,j,k}^{n-1} - 2u_{ij,k}^{n-1} + u_{i-1,j,k}^{n-1}}{\cos^2 \phi \Delta \lambda_i^2} + \frac{u_{ij+1,k}^{n-1} - 2u_{ij,k}^{n-1} + u_{ij-1,k}^{n-1}}{\Delta \phi_j^2} + \tan \phi \frac{u_{ij+1,k}^{n-1} - u_{ij-1,k}^{n-1}}{2\Delta \phi_j} \right),$$

$$[K_m(u^{n-1})_z]_z = \frac{1}{\Delta z_k} \left[(K_m)_{ij,k} \left(\frac{u_{ij,k+1}^{n-1} - u_{ij,k}^{n-1}}{\Delta z_k} \right) - (K_m)_{ij,k-1} \left(\frac{u_{ij,k}^{n-1} - u_{ij,k-1}^{n-1}}{\Delta z_k} \right) \right].$$

Note that pressure is expressed in terms of forward barotropic surface pressure and centered baroclinic pressure. Vertical mixing is parameterized based on Pacanowski and Philander (1981). Coriolis terms are updated by a trapezoidal approach. The predicted cell-centered velocities are interpolated to the faces using the fourth-order approximation (Sanderson and Brassington 1998). Similar procedure is applied to the conservation equations for final potential temperature and salinity.

2) Corrector step: Forward surface pressure used in the predictor step requires further correction (i.e., centered time stepping) to achieve the final flow fields:

$$U_{i+1/2,j,k}^{n+1} = \hat{U}_{i+1/2,j,k}^{n+1} + \delta U_{i+1/2,j,k}^{n+1}, \quad (17)$$

$$V_{ij+1/2,k}^{n+1} = \hat{V}_{ij+1/2,k}^{n+1} + \delta V_{ij+1/2,k}^{n+1}, \quad (18)$$

where

$$\begin{aligned} \delta U_{i+1/2,j,k}^{n+1} &= -\frac{2\Delta t}{\rho_0 R \cos \phi} \frac{\partial}{\partial \lambda} (p_s^n - p_s^{n-1}) \\ &= -\frac{2\Delta t}{\rho_0 R \cos \phi} \frac{\partial}{\partial \lambda} (\delta p_s^n), \end{aligned} \quad (19)$$

$$\delta V_{ij+1/2,k}^{n+1} = -\frac{2\Delta t}{\rho_0 R} \frac{\partial}{\partial y} (p_s^n - p_s^{n-1}) = -\frac{2\Delta t}{\rho_0 R} \frac{\partial}{\partial y} (\delta p_s^n). \quad (20)$$

Surface pressure corrections and corresponding face velocity adjustments are obtained by imposing the vertically integrated continuity equation:

$$\begin{aligned} \frac{2\Delta t}{\rho_0 R^2 \cos \phi} \left[\frac{\partial}{\partial \lambda} \left(\frac{h}{\cos \phi} \frac{\partial \delta p_s^n}{\partial \lambda} \right) + \frac{\partial}{\partial \phi} \left(h \frac{\partial \delta p_s^n}{\partial \phi} \right) \cos \phi \right] \\ = \hat{w}_{-h}^{n+1}, \end{aligned} \quad (21)$$

where the last term is a convenient shorthand notation and can be expressed as

$$\begin{aligned} \hat{w}_{-h}^{n+1} &= \frac{1}{R \cos \phi} \left(\frac{\partial}{\partial \lambda} \int_{-h}^0 \hat{U}^{n+1} dz \right. \\ &\quad \left. + \frac{\partial}{\partial \phi} \int_{-h}^0 \hat{V}^{n+1} \cos \phi dz \right). \end{aligned} \quad (22)$$

The resulting Poisson equation is efficiently solved using the error vector propagation (EVP) method (Roache 1995) or other iterative solvers [e.g., the bi-conjugate gradient stabilized method (BiCGSTAB); see Van der Vorst 1992]. The changes for cell-centered velocity are then updated (see Young et al. 2012 or TIMCOM's user's manual for details). Once the surface pressures and horizontal velocities are fully updated, vertical velocity is determined diagnostically from the continuity equation, followed by the third-order RAW filtering Eqs. (2)–(3) for the flow variables in order to advance in time (Williams 2009).

4. Results and discussion

The new RAW filtering algorithm in TIMCOM is examined through the simulation of (i) coastal Kelvin waves that affect the thermocline in large lakes or oceans (see Wang and Mooers 1976) and (ii) global oceanic circulation that plays an important role in the

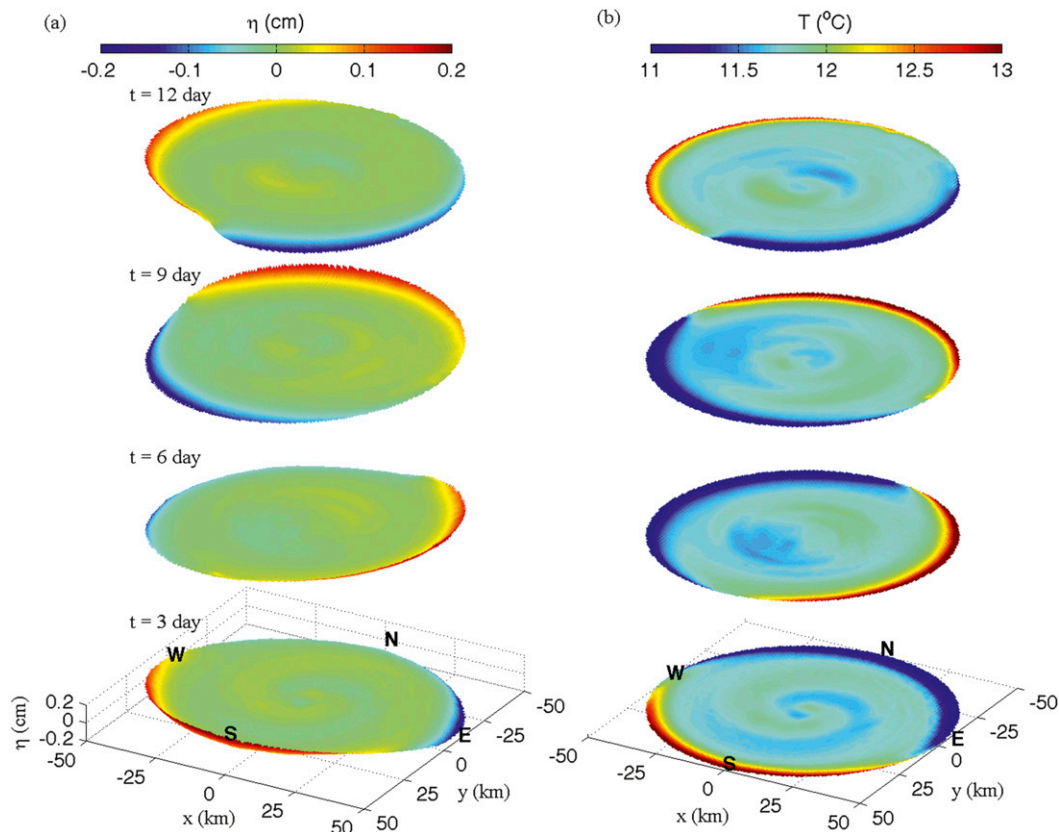


FIG. 6. The modeled (a) surface height and (b) 10-m depth temperature of the coastally trapped internal Kelvin wave propagating around the lake at 3, 6, 9, and 12 days.

earth climate system (Gill 1982). The former case shows significant reduction of numerical truncation error. For the latter case, an improved structure of some major current systems in the global simulation indicates a better prediction of the Atlantic meridional overturning circulation.

a. Coastal Kelvin waves

We simulate the propagation of small-amplitude Kelvin waves in an idealized lake (Beletsky et al. 1997) using TIMCOM. The basin has a circular shape with a diameter of 100 km. A constant depth of 100 m is considered to exclude the topography effect. The Coriolis parameter is set to $f = 10^{-4} \text{ s}^{-1}$ (i.e., the site location at 42°N). The initial temperature is 20°C at the upper 5-m mixed layer and linearly decreases to 5°C at the bottom layer across a 10-m thermocline. To generate the internal Kelvin waves, a southward wind stress increases linearly from 0 to 0.01 N m^{-2} over 18 h and then remains constant for another 6 h, followed by decreasing to 0 in the next 5 h.

The computational domain is horizontally discretized by a set of 160×160 uniform Cartesian grids

($\Delta x = \Delta y = 625 \text{ m}$), which is enough to resolve the nearshore dynamics (Bennett 1977). Twenty-five stretching layers (1.0/14.0-m thickness at the top/bottom layers) are employed vertically. The time step Δt is 300 s to ensure that the Courant number is less than the suggested value [i.e., $Co = C\Delta t/\Delta x = 0.17 < 0.20$, where Co is estimated using the inviscid linear wave speed $C = 0.36 \text{ m s}^{-1}$ (Csanady 1968)]. The simulation is run up to 12 days. The parameters in the RAW filter are $\nu = 0.1$ and $\alpha = 0.53$ based on our previous analysis.

Figure 6 shows the coastally trapped response of the thermocline at $t = 3, 6, 9,$ and 12 days based on the simulated surface height and temperature at 10-m depth using the RAW-filtered leapfrog scheme. Because of the influence of favorable wind stress and Earth’s rotation, the surface water flows southwest and piles up at the lake boundaries, resulting in the downwelling (upwelling) of warmer (colder) waters along the southwestern (northeastern) shorelines. When the wind subsides, the balance between pressure gradient and Coriolis force causes the cyclonic progression of tilted surface and upwelling/downwelling regions. Figure 7 further shows a snapshot ($t = 12$ days) of the surface velocity vectors, underlying

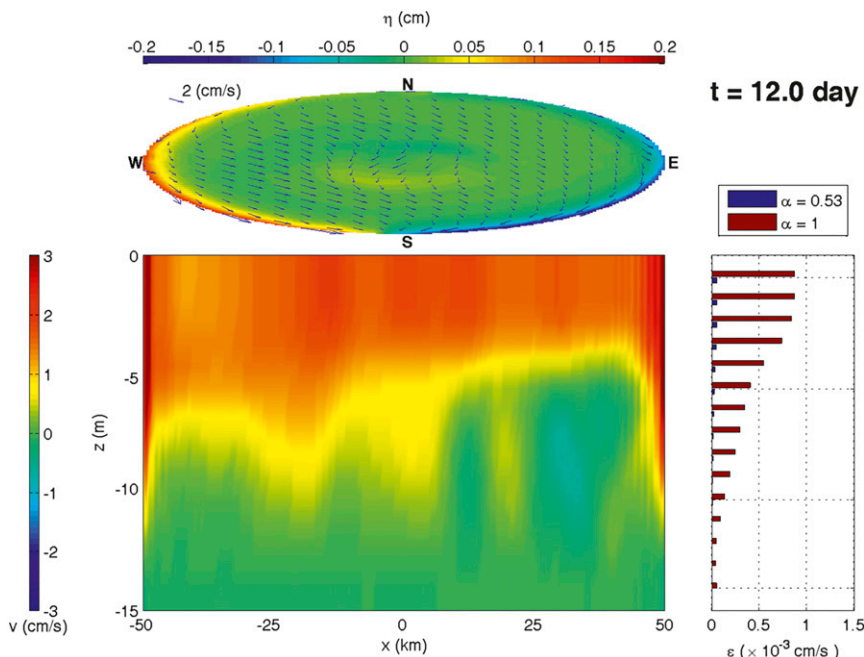


FIG. 7. A snapshot ($t = 12$ days) of the modeled surface velocity vectors, underlying positive southward velocity across the upper part of the west–east section (i.e., $y = 0$ km) of internal Kelvin waves, and the residual of the mean-state conservation after filtering.

positive southward velocity across upper part of the west–east section (i.e., $y = 0$ km), and the residual of the mean-state conservation after filtering: $\varepsilon_k = \sum_{j=1}^{160} |(\overline{v_{80,j,k}^{n-1}} + \overline{v_{80,j,k}^{n+1}})/3 - (\overline{v_{80,j,k}^n} + \overline{v_{80,j,k}^{n+1}})/3|$, where the overbars are used to indicate the filtered flow fields at the centered (n) and forward ($n + 1$) time levels before advancing to the next time step. It is clear that the residual of the mean-state conservation is reduced significantly using the RAW-filtered leapfrog scheme (see the right box in Fig. 7). While the conservation states are relatively different, the RAW ($\alpha = 0.53$) and RA filters ($\alpha = 1.0$) yield almost identical patterns in this dissipation case because the active physical instability dominates and potentially interferes with the numerical instability.

b. Global oceanic circulation

TIMCOM (parallel version; see Tseng and Chien 2011) is then applied to simulate global oceanic circulation. The model domain covers the entire globe from 72°S to 72°N . The depth is derived from the Elevation Data for Areas Greater than 50 degrees North (ETOPO5) bathymetry data. Initial potential temperature and salinity fields are specified using climatology of Levitus and Boyer (1994). Density, a function of potential temperature, salinity, and pressure, is calculated by a nonlinear equation of state (Tseng et al. 2005). The Scatterometer Climatology of Ocean Winds (SCOW) is used to drive

the circulations (Risien and Chelton 2008). Surface sources of heat and freshwater are specified by a non-damping approach (Dietrich et al. 2004a). The simulation is carried out on a $1/4^\circ$ Mercator grid (1440×720 horizontal cells) with 50 stretched vertical layers. The northern and southern closed boundaries are nudged toward climatology. We take the time step $\Delta t = 240$ s rather than a much longer value commonly used in ocean modeling [e.g., $\Delta t = 3000$ s for the GFDL MOM $1^\circ \times 1/3^\circ$ simulation (Pacanowski and Griffies 1999)]. Based on this time step setting, the accumulated amplitude errors are about 0.01% over a long-term integration and no $2\Delta x$ wave instability appears since the corresponding Courant number is only $O(0.01)$ (i.e., $\text{Co} = C\Delta t/\Delta x \ll 0.20$ with the speed $C = 3 \text{ m s}^{-1}$ for the internal gravity wave or $C = 1.5 \text{ m s}^{-1}$ for the surface current; Bryan 1984). The total length of the simulation is up to 20 yr to obtain a quasi-equilibrium ocean state.

We compare the performances between the RAW and RA filtered leapfrog schemes (i.e., $v = 0.1$ and $\alpha = 0.53$ or 1.0). Figure 8a shows the RAW ($\alpha = 0.53$) filtered leapfrog model results of the last 10-yr-averaged surface current velocity, presenting clear Kuroshio fronts, Gulf Stream separation, and significant ring generation associated with shear instability in the Agulhas Current. General features of major current systems are well captured and qualitatively similar to the drifter or satellite observations (e.g., Lumpkin and Pazos 2007)

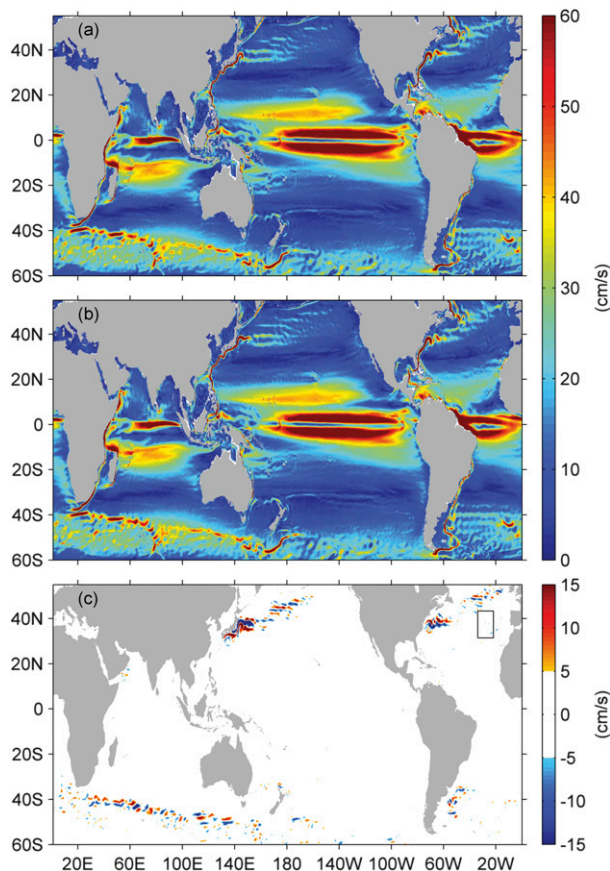


FIG. 8. Modeled 10-yr-averaged surface current velocity from (a) RAW ($\alpha = 0.53$) and (b) RA ($\alpha = 1.0$) filtered leapfrog schemes. (c) The difference between RAW and RA results.

except the common overshoot of the separation location in an eddy-permitting model. The surface current velocity from RA ($\alpha = 1.0$) filtered leapfrog scheme is shown in Fig. 8b. Note that no exact solution is available to quantify amplitude improvement in the model results. The differences between these two simulations $\Delta V = V_{\text{RAW}} - V_{\text{RA}}$ are presented in Fig. 8c. The mixed positive–negative pattern is similar to the previous comparison of surface elevation between the accurate solutions ($\alpha = 0.53$) and underestimated crest/trough ($\alpha = 1.0$). Particularly note that a major discrepancy (up to 30% V_{RAW}) can be found in the western boundary currents and Antarctic Circumpolar Current (ACC) due to the Agulhas retroflection. The differences are mainly associated with the shifted locations of the current systems and their separation points, which are sensitive to several potential contributions (Dietrich et al. 2004b; Chassignet and Marshall 2008). These areas are also well known to be subjected to several instability mechanisms and topography, especially the Gulf Stream path. The Agulhas leakage and its low-frequency variability (Beal et al. 2011) may contribute to the instability in the

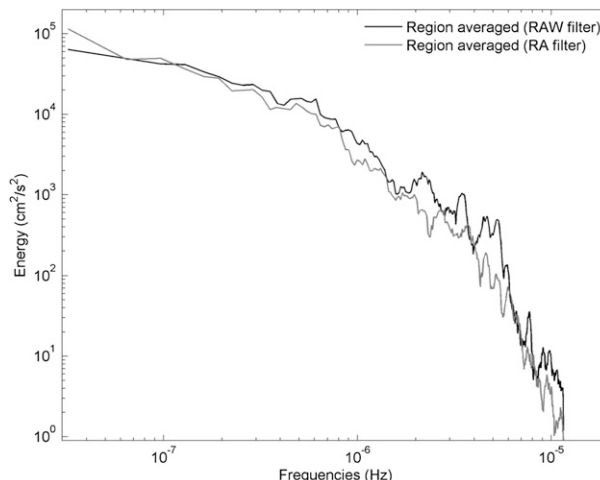


FIG. 9. Energy spectrum of the modeled velocity field around the central North Atlantic [black lines: $\alpha = 0.53$, gray lines: $\alpha = 1.0$, solid lines: regionally averaged velocity (see Fig. 8c for the region)].

modeled ACC. The overall results indicate that the numerical instability may interfere with the physical one for some areas in the realistic ocean application.

Figure 9 further examines the last-year model results and compares the regionally averaged energy spectrum around the central North Atlantic (the black box in Fig. 8c), where there is slight difference between the RAW and RA filters. It can be found that the low-frequency signals associated with the mesoscale motions are quite similar but the high-frequency small-scale oscillations (10^{-6} – 10^{-5} Hz, in the range of hours to weeks) obtained by the RAW-filtered leapfrog scheme are more conservative (or energetic). The difference of the small-scale fluctuations could result from the path (or unsteadiness) of the predicted current system (e.g., the Gulf Stream), which could be significantly influenced by the numerical dissipation of the time-advancing scheme. These results are quite similar to the effects of physical dissipation (Dietrich et al. 2004b). Overall, the most affected frequency/time scale in our simulations is consistent with the finding in the SPEEDY atmospheric model (i.e., the greatly improved 5-day forecasting; Amezcua et al. 2011).

The annual-averaged sea surface height and surface current velocity of the North Atlantic also shows that the third-order RAW-filtered leapfrog scheme (Fig. 10a) resolves oceanic fronts (denser contours along the main pathway) better than the RA-filtered scheme (Fig. 10b). Improved Gulf Stream structure and ACC may indicate better prediction of the Atlantic meridional overturning circulation, which is a key component in the global ocean climate. The impact of the time-stepping scheme on the global ocean climate system requires a more careful evaluation next. Overall, the RAW filtering algorithm is strongly recommended for the ocean general circulation

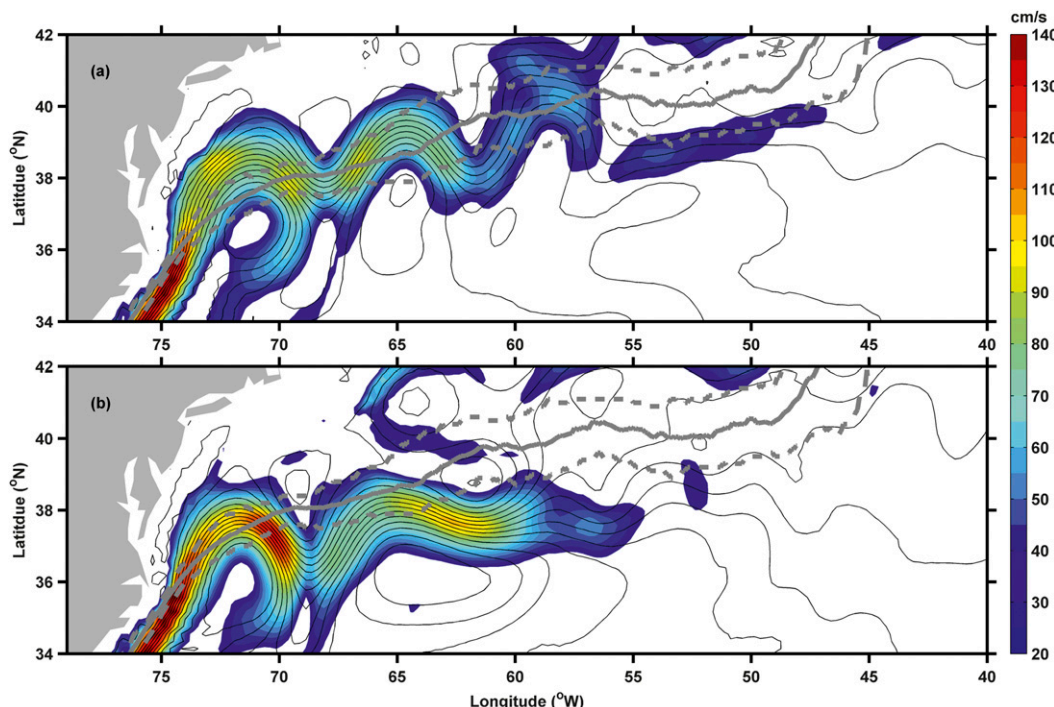


FIG. 10. Modeled annual-averaged sea surface height (contours) and current velocity (colors) at the North Atlantic Ocean, obtained from (a) RAW ($\alpha = 0.53$) and (b) RA ($\alpha = 1.0$) filtered leapfrog schemes [gray lines: Gulf Stream pathway $\pm 1\sigma$ from Hurlburt and Hogan (2008)].

models based upon the current results. Using the RAW-filtered leapfrog scheme, accurate representation of the ocean state (e.g., proper modeling of mass/thermal transport in boundary current system) can lead to more realistic regional and global climate study (Kawabe 1995; Yoshinari et al. 2004; Miyazawa et al. 2008; Tseng et al. 2012).

5. Summary

This study applies the RAW filtering algorithm (Williams 2009; Amezcua et al. 2011) to a multiscale oceanic circulation model, TIMCOM (Young et al. 2012). Characteristics of the RAW filter are carefully examined and analyzed through two benchmark tests: the model problem-oscillation equation with further consideration of the dissipation effect and one-dimensional linearized shallow-water equations (Durrant 1991; Sun 2010). The issue of computational $2\Delta x$ wave instability is also addressed. The recommended filtering parameters and time step criteria are $\alpha = 0.53$, $\nu = 0.1$, and $Co \leq 0.2$ for accurate ocean modeling in practice. All of these are necessary conditions in order to minimize the truncation errors.

TIMCOM is then applied to simulate the coastally trapped internal Kelvin waves (Beletsky et al. 1997) and global circulation patterns (Tseng and Chien 2011), showing the significant advantage of the RAW filter in

short- and long-term time integration. Particularly, more energetic velocity field and stronger sea surface height gradients are maintained in the simulated ocean states (e.g., the Gulf Stream) using the RAW filter, better predicting mass/thermal transport in the major current system, which is critical to regional and global ocean climate (Tseng et al. 2012). Based on our analysis and simulation results, the RAW filter with recommended parameters is strongly suggested for the simulation of global ocean circulation when leapfrog-type time advancing is employed. Currently, coupling TIMCOM within the community earth system model (CESM) is under way to achieve more realistic ocean climate modeling. Updated results will be reported in the near future.

Acknowledgments. The financial supports provided by the National Science Council, Taiwan (Grants 100-2628-M-002-010-MY2 and 100-2811-M-002-140) and the Climate and Global Dynamics Division, National Center for Atmospheric Research are greatly appreciated. We also thank the anonymous reviewers and the editor, Dr. Dale R. Durran, for their constructive and helpful comments.

REFERENCES

- Amezcua, J., E. Kalnay, and P. D. Williams, 2011: The effects of the RAW filter on the climatology and forecast skill of the SPEEDY model. *Mon. Wea. Rev.*, **139**, 608–619.

- Asselin, R., 1972: Frequency filter for time integrations. *Mon. Wea. Rev.*, **100**, 487–490.
- Beal, L. M., and Coauthors, 2011: On the role of the Agulhas system in ocean circulation and climate. *Nature*, **472**, 429–436.
- Beletsky, D., W. P. O'Connor, D. J. Schwab, and D. E. Dietrich, 1997: Numerical simulation of internal Kelvin waves and coastal upwelling fronts. *J. Phys. Oceanogr.*, **27**, 1197–1215.
- Bennett, J. R., 1977: A three-dimensional model of Lake Ontario's summer circulation. I: Comparison with observations. *J. Phys. Oceanogr.*, **7**, 591–601.
- Bryan, K., 1984: Accelerating the convergence of equilibrium of ocean-climate models. *J. Phys. Oceanogr.*, **14**, 666–673.
- Chassignet, E. P., and D. P. Marshall, 2008: Gulf Stream separation in numerical ocean models. *Ocean Modeling in an Eddying Regime, Geophys. Monogr.*, Vol. 177, Amer. Geophys. Union, 39–61.
- Csanady, G. T., 1968: Wind-driven summer circulation in the Great Lakes. *J. Geophys. Res.*, **73**, 2579–2589.
- Dietrich, D. E., and J. J. Wormeck, 1985: An optimized implicit scheme for compressible reactive gas flow. *Numer. Heat Transfer*, **8**, 335–348.
- , R. L. Haney, V. Fernandez, S. Josey, and J. Tintore, 2004a: Air-sea fluxes based on observed annual cycle surface climatology and ocean model internal dynamics: A precise, non-damping zero-phase-lag approach applied to the Mediterranean Sea. *J. Mar. Syst.*, **52**, 145–165.
- , A. Mehra, R. L. Haney, M. J. Bowman, and Y. H. Tseng, 2004b: Dissipation effects in North Atlantic Ocean modeling. *Geophys. Res. Lett.*, **31**, L05302, doi:10.1029/2003GL019015.
- Durran, D. R., 1991: The third-order Adams–Bashforth method: An attractive alternative to leapfrog time differencing. *Mon. Wea. Rev.*, **119**, 702–720.
- , and P. N. Blossey, 2012: Implicit–explicit multistep methods for fast-wave–slow-wave problems. *Mon. Wea. Rev.*, **140**, 1307–1325.
- Gill, A. E., 1982: *Atmosphere–Ocean Dynamics*. International Geophysics Series, Vol. 30, Academic Press, 662 pp.
- Hurlburt, H. E., and P. J. Hogan, 2008: The Gulf Stream pathway and the impacts of the eddy-driven abyssal circulation and the Deep Western Boundary Current. *Dyn. Atmos. Oceans*, **45**, 71–101.
- Kantha, L., and C. Clayson, 2000: *Numerical Models of Oceans and Oceanic Processes*. International Geophysics Series, Vol. 66, Academic Press, 750 pp.
- Kar, S. K., 2006: A semi-implicit Runge–Kutta time-difference scheme for the two-dimensional shallow-water equations. *Mon. Wea. Rev.*, **134**, 2916–2926.
- Kawabe, M., 1995: Variations of current path, velocity, and volume transport of the Kuroshio in relation with the large meander. *J. Phys. Oceanogr.*, **25**, 3103–3117.
- Kurihara, Y., 1965: On the use of implicit and iterative methods for the time integration of the wave equation. *Mon. Wea. Rev.*, **93**, 33–46.
- Levitus, S., and T. P. Boyer, 1994: *Temperature*. Vol. 4, *World Ocean Atlas 1994*, NOAA Atlas NESDIS 4, 117 pp.
- Lumpkin, R., and M. Pazos, 2007: Measuring surface currents with surface velocity program drifters: The instrument, its data, and some recent results. *Lagrangian Analysis and Prediction of Coastal and Ocean Dynamics*, A. Griffa et al., Eds., Cambridge University Press, 39–67.
- Magazenkov, L. N., 1980: Time integration schemes for fluid dynamics equations, effectively damping the high frequency components (in Russian). *Tr. Gl. Geofiz. Obs.*, **410**, 120–129.
- Mesinger, F., and A. Arakawa, 1976: *Numerical Methods Used in Atmospheric Models*. Global Atmosphere Research Program (GARP) Publication Series 17, Vol. I, GARP, 64 pp.
- Miyazawa, Y., T. Kagimoto, X. Guo, and H. Sakuma, 2008: The Kuroshio large meander formation in 2004 analyzed by an eddy-resolving ocean forecast system. *J. Geophys. Res.*, **113**, C10015, doi:10.1029/2007JC004226.
- Molteni, F., 2003: Atmospheric simulations using a GCM with simplified physical parameterizations. I. Model climatology and variability in multi-decadal experiments. *Climate Dyn.*, **20**, 175–191.
- Pacanowski, R. C., and S. G. H. Philander, 1981: Parameterization of vertical mixing in numerical models of tropical ocean. *J. Phys. Oceanogr.*, **11**, 1443–1451.
- , and S. M. Griffies, 1999: The MOM 3 manual. NOAA/Geophysical Fluid Dynamics Laboratory, Princeton, NJ, 680 pp.
- Pfeffer, R., I. Navon, and X. Zou, 1992: A comparison of the impact of two time-differencing schemes on the NASA GLAS climate model. *Mon. Wea. Rev.*, **120**, 1381–1393.
- Risien, C. M., and D. B. Chelton, 2008: A global climatology of surface wind and wind stress fields from eight years of QuikSCAT scatterometer data. *J. Phys. Oceanogr.*, **38**, 2379–2413.
- Roache, P. J., 1995: *Elliptic Marching Methods and Domain Decomposition*. CRC Press, 208 pp.
- , and D. E. Dietrich, 1988: Evaluation of the filtered Leapfrog–Trapezoidal time integration method. *Numer. Heat Transfer*, **14**, 149–164.
- Sanderson, B. G., and G. Brassington, 1998: Accuracy in the context of a control-volume model. *Atmos.–Ocean*, **36**, 355–384.
- Solomon, S., D. Qin, M. Manning, Z. Chen, M. Marquis, K. Averyt, M. Tignor, and H. L. Miller Jr., Eds., 2007: *Climate Change 2007: The Physical Science Basis*. Cambridge University Press, 996 pp.
- Sun, W. Y., 2010: Instability in leapfrog and forward-backward schemes. *Mon. Wea. Rev.*, **138**, 1497–1501.
- Teixeira, J., C. A. Reynolds, and K. Judd, 2007: Time step sensitivity of nonlinear atmospheric models: Numerical convergence, truncation error growth, and ensemble design. *J. Atmos. Sci.*, **64**, 175–189.
- Tseng, Y. H., and M. H. Chien, 2011: Parallel Domain-decomposed Taiwan Multi-scale Community Ocean Model (PD-TIMCOM). *Comput. Fluids*, **45**, 77–83.
- , D. E. Dietrich, and J. H. Ferziger, 2005: Regional circulation of the Monterey Bay region: Hydrostatic versus nonhydrostatic modeling. *J. Geophys. Res.*, **110**, C09015, doi:10.1029/2003JC002153.
- , M. L. Shen, S. Jan, D. E. Dietrich, and C. P. Chiang, 2012: Validation of the Kuroshio Current system in the dual-domain Pacific Ocean model framework. *Prog. Oceanogr.*, **105**, 102–124.
- Van der Vorst, H. A., 1992: Bi-CGSTAB: A fast and smoothly converging variant of Bi-CG for the solution of non-symmetric linear systems. *SIAM J. Sci. Stat. Comput.*, **13**, 631–644.
- Wang, D. P., and C. N. K. Mooers, 1976: Coastal-trapped waves in a continuously stratified ocean. *J. Phys. Oceanogr.*, **6**, 853–863.
- Williams, P. D., 2009: A proposed modification to the Robert–Asselin time filter. *Mon. Wea. Rev.*, **137**, 2538–2546.
- Wood, R. A., A. B. Keen, J. F. B. Mitchell, and J. M. Gregory, 1999: Changing spatial structure of the thermohaline circulation in response to atmospheric CO₂ forcing in a climate model. *Nature*, **399**, 572–575.
- Yoshinari, H., M. Ikeda, K. Tanaka, and Y. Masumoto, 2004: Sensitivity of the interannual Kuroshio Transport variation south of Japan to wind dataset in OGCM calculation. *J. Oceanogr.*, **60**, 341–350.
- Young, C. C., Y. H. Tseng, M. L. Shen, Y. C. Liang, M. H. Chien, and C. H. Chien, 2012: Development of the Taiwan Multi-scale Community Ocean Model (TIMCOM). *Environ. Modell. Software*, **38**, 214–219.